Size-based hydrodynamic rare tumor cell separation in curved microfluidic channels

Jiashu Sun,[1,a)] Chao Liu,[2,a)] Mengmeng Li,[1,a)] Jidong Wang,[1] Yunlei Xianyu,[1] Guoqing Hu,[2,b)] and Xingyu Jiang[1,b)]
[1]*CAS Key Lab for Biological Effects of Nanomaterials and Nanosafety, National Center for NanoScience and Technology, Beijing 100190, China*
[2]*LNM, Institute of Mechanics, Chinese Academy of Sciences, Beijing 100190, China*

(Received 1 September 2012; accepted 24 October 2012; published online 7 January 2013)

In this work, we propose a rapid and continuous rare tumor cell separation based on hydrodynamic effects in a label-free manner. The competition between the inertial lift force and Dean drag force inside a double spiral microchannel results in the size-based cell separation of large tumor cells and small blood cells. The mechanism of hydrodynamic separation in curved microchannel was investigated by a numerical model. Experiments with binary mixture of 5- and 15-μm-diameter polystyrene particles using the double spiral channel showed a separation purity of more than 95% at the flow rate above 30 ml/h. High throughput (2.5×10^8 cells/min) and efficient cell separation (more than 90%) of spiked HeLa cells and $20\times$ diluted blood cells was also achieved by the double spiral channel. © *2013 American Institute of Physics*. [http://dx.doi.org/10.1063/1.4774311]

I. INTRODUCTION

Tumor cell separation and enrichment have attracted significant attention because of its important applications in cancer research, biomedical diagnostics, and treatment strategies.[1,2] Circulating tumor cells (CTCs) found in peripheral blood are proven to be correlated with aggressiveness of the tumor, and have potential to serve as a marker of cancer diagnosis and therapeutic treatment monitoring.[3] However, conventional detection methods including immunostaining and flow cytometry cannot make reliable detection of CTCs because of the extremely low numbers of CTCs in peripheral blood (as few as 1 CTC/ml).[4] Therefore, a separation step of CTCs from whole blood is prerequisite to improve the accuracy and sensitivity of detection.[5]

Microfluidic techniques, an effective tool for cell manipulation and detection, have been intensively involved for tumor cell separation and enrichment from peripheral blood samples.[6–12] One commonly used parameter for CTC enrichment is the cell size, as most CTCs are epithelial tumor cells of 13 to 25 μm in diameter, larger than the surrounding blood cells.[13] Based on this physical criteria, Zheng and collaborators developed a MEMS-based parylene membrane microfilter device with pore size of 8 μm to enrich CTC on filter with ~90% recovery within 10 min.[14,15] However, these microfiltration systems faced the challenge of membrane clogging due to the high blood concentration.[16] Alternatively, different size-based separation mechanisms, including dielectrophoresis (DEP), magnetophoresis, acoustophoresis, and optophoresis, have also been applied to separate the tumor and blood cells using microfluidic devices.[17–19] For example, DEP-based separation is to induce size-dependent transverse DEP migration of cells that are exposed to a non-uniform electric field, thus, separating the large tumor cells from the surrounding small cells.[20] However, those phoresis-based cell sorters suffered from the problems of low throughput, complicated integration of external force fields and possible loss of cell viability.

[a)]J. Sun, C. Liu, and M. Li contributed equally to this work.
[b)]Authors to whom correspondence should be addressed. Electronic addresses: guoqing.hu@imech.ac.cn and xingyujiang@nanoctr.cn.

In comparison, hydrodynamic-based microfluidic cell separation techniques that solely rely on the manipulation of fluids in small length scale have been applied for efficient tumor cell separation without labeling and external force fields.[21] By inducing the hydrodynamic effects inside the particular micro-geometries, e.g., curved serpentine or spiral configuration, tumor or blood cell separation is achieved, whereby the trajectories and equilibrium positions of cells are size dependent. For example, using differential inertial focusing in asymmetric curving channels, Di Carlo and co-workers demonstrated the label-free separation of platelets from diluted blood cells at a high flow rate.[22] Moreover, the spiral microfluidic device was applied to enrich tumor cells from blood based on competition between inertial lift and Dean drag forces.[23,24] More recently, Bhagat and collaborators designed a single inlet rectangular microchannel patterned with a contraction-expansion array to isolate CTCs from blood by hydrodynamic forces.[13] Although substantial investigations of hydrodynamic separation in irregular micro-geometries have been done previously, the theory and the mechanism of particle/cell dynamics are still far away from being conclusive, and a better understanding of hydrodynamic separation mechanism is desired for the application of hydrodynamic-based CTC separation.

Here, we propose a double spiral microfluidic channel that can continuously separate tumor and blood cells based on size difference with throughput comparable to conventional techniques. A numerical scheme was developed to investigate the hydrodynamic effects in double spiral channel by modeling the movement of different size particles. The microfluidic device was first characterized with the binary mixture of 5- and 15-μm-diameter polystyrene particles at different flow rates. Moreover, highly efficient separation of HeLa cells from the $20\times$ diluted human blood cells with the initial tumor-to-blood cell ratio of 8×10^{-7} was demonstrated at the throughput of 2.5×10^{8} cells/min.

II. THEORY AND NUMERICAL METHODS

Many factors, including geometries of channel, flow conditions, and properties of suspending liquid medium, influence the performance of the microfluidic particle/cell sorting devices. We design a double spiral microchannel with 6-loop for each direction for particle/cell manipulation, as illustrated in Fig. 1(a). At a relatively high Reynolds number, the non-uniform inertia of fluid inside the curved channel results in a secondary cross-section flow, termed as Dean flow (Fig. 2). The equilibrium positions of particles inside the channel are determined by the competition between hydrodynamic (drag and lift) forces acting on the particles in high-velocity flows. To describe the motion of particles in closed microchannels, two dimensional Reynolds numbers are introduced here: the channel Reynolds number (Re_C) and the particle Reynolds number (Re_P)

$$\mathrm{Re}_C = \frac{\rho U_m D_h}{\mu},$$
$$\mathrm{Re}_P = \mathrm{Re}_C \frac{a^2}{D_h^2} = \frac{\rho U_m a^2}{\mu D_h}, \tag{1}$$

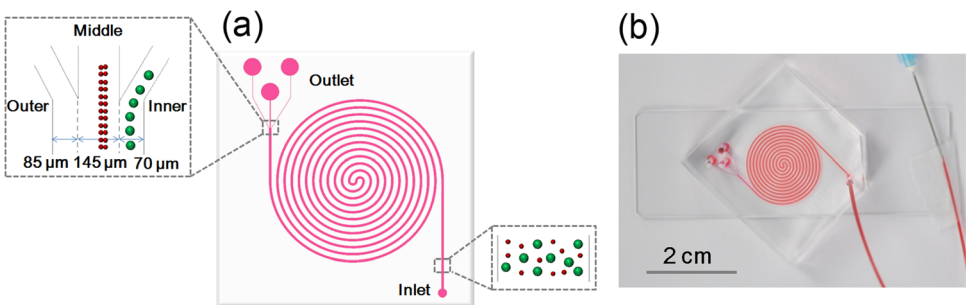

FIG. 1. (a) Schematics of the microfluidic cell sorter containing 6-loop double spiral microchannel for particle/cell separation. (b) Picture of the assembled cell sorter.

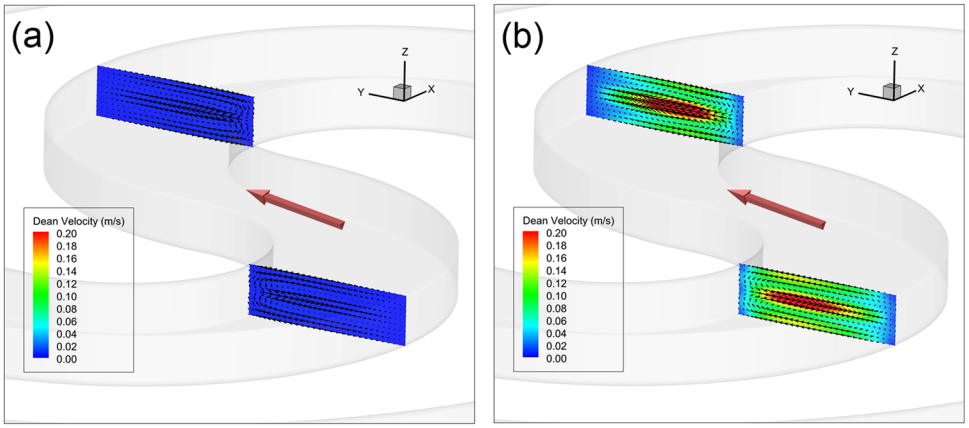

FIG. 2. Comparison of the Dean vortices and their magnitude at (a) 10 ml/h, and (b) 60 ml/h at the S-shape junction. The small arrows represent the velocity vector projected onto the cross-section and color contours represent the magnitude of the Dean flow velocity. The big red arrow indicates the flow direction.

where U_m is the maximum velocity within microchannel, ρ and μ are the density and the dynamic viscosity of the fluid, respectively, D_h is the hydrodynamic diameter of microchannel (four times the channel cross section divided by the perimeter), and a is the particle diameter. Inertial lift force dominates the particle traffic at finite but low Reynolds numbers. Schonberg and Hinch[25] and more recently, Asmolov[26] calculated the force on a neutrally buoyant particle in a two dimensional quadratic flow for Reynolds numbers up to 1500. At small particle Reynolds number $\mathrm{Re}_P \ll 1$, the magnitude of the lift force responsible for movement away from the channel center and walls, is given by

$$F_L = \frac{\mu^2}{\rho}\mathrm{Re}_P^2 f_C(\mathrm{Re}_C, x_C), \tag{2}$$

where the left coefficient, f_C is a function of the channel Reynolds number Re_C, and the particle position x_C within the cross-section of the channel (the distance to the channel center).

In addition, the curvature of the present double-spiral microchannel creates additional transverse drag force on particles by inducing secondary flows normal to the streamwise direction, which is described by a dimensionless Dean number (De)

$$De = \mathrm{Re}_C\sqrt{D_h/R}, \tag{3}$$

where R is the curvature radius. The magnitude of the Dean drag force on suspended particles due to the secondary flow can be written as[27]

$$F_D \sim \rho U^2 a D_h^2/R. \tag{4}$$

A comprehensive understanding of the flow field and the particle behavior is crucial for a better design of particle/cell separation devices. Although substantial investigations have been done previously, the theory and the mechanism of particle dynamics, even within a seemly simple straight channel, are still far away from being conclusive. Here, we present a Lagrangian particle tracking technique called discrete phase model (DPM) to model the particle motion in the 3-D double spiral microchannel. In our experiments, the particle concentration is very low. Therefore, it is reasonable to assume that presence of the particles does not significantly influence fluid properties and thus the flow fields. The steady flow field is first obtained by solving the impressible Navier-Stokes equations

$$\nabla \cdot \vec{v} = 0,$$
$$\rho \vec{v} \cdot \nabla \vec{v} = -\nabla p + \nabla \cdot [\mu(\nabla \vec{v} + \nabla \vec{v}^{T})], \tag{5}$$

where $\vec{v}$ is the velocity vector and p is the static pressure. Subsequently, a particle trajectory is obtained by integrating the force balance based on Newton's second law of motion

$$\frac{d\vec{v}_p}{dt} = \frac{18\mu}{\rho_P a^2}\frac{C_D \mathrm{Re}_s}{24}(\vec{v} - \vec{v}_P) + \frac{\vec{g}(\rho_P - \rho)}{\rho_P} + \frac{1}{2}\frac{\rho}{\rho_P}\frac{d(\vec{v} - \vec{v}_P)}{dt} + \frac{F_L}{\frac{1}{6}\pi a^3 \rho_P}, \tag{6}$$

where t is the time, $\vec{v}_P$ is the velocity vector of the particles, and ρ_P is the density of particle. More details can be found in our pervious publication.[24]

All the numerical simulations are carried out by the commercial CFD software FLUENT 6.4 (Ansys Inc.). First, the Navier-Stokes equations for flow fields without particles are solved using a second order upwind scheme, along with the SIMPEC algorithm for pressure-velocity coupling. Nonslip boundary conditions are implemented on the channel walls. A pressure boundary condition is applied for the channel inlet to match the flow rates used in experiments while an atmospheric pressure is fixed for the outlet. The trajectories of particles are then tracked using the DPM method based on the obtained flow fields. The inertial lift force for the particles is added using a user defined function (UDF) in FLUENT.

III. MATERIALS AND METHODS

The separation chip is a 6-loop double spiral microchannel of 300 μm wide and 85 μm high with one inlet and three outlets, as depicted in Fig. 1(a). The channel connected with the inlet first spirals in the counterclockwise direction, changes its direction through an S-shape center junction, spirals out, and ends with the trifurcated outlet. The outlets from right to left are termed as inner outlet (70 μm wide), middle outlet (145 μm wide), and outer outlet (85 μm wide). The distance between two adjunction loops is 450 μm. The total length of the double spiral channel is 334 mm. The 6-loop single spiral channel has the same channel width and height, and rotates in the clockwise direction beginning from the inlet at the center. The trifurcated outlet of the single spiral channel has the same dimensions as the double one.

The microfluidic device was fabricated using standard soft-lithography techniques with SU8 master mold on a silicon substrate.[28,29] After the polydimethylsiloxane (PDMS) slab was peeled off from the mold, four ports at the inlet and outlets were punched through the PDMS with a flat tip needle. The PDMS slab was then bonded with a glass substrate (25 mm × 75 mm) post oxygen plasma treatment.[30] The plastic tube was inserted through the inlet port and glued by the liquid PDMS on the top of device. The assembled device was finally placed into an oven at 70 °C for 30 min to cure the liquid PDMS and increase bonding (Fig. 1(b)).

In the experiment of separating the particle mixture, the double/single spiral microchannel was first primed with deionized water. Fluorescent labeled 5-μm-diameter (red) and 15-μm-diameter (green) polystyrene microspheres were purchased from Phosphorex, Inc. The suspension of 5 μm particles or 15 μm particles was diluted in deionized water containing 0.1% w/v Tween 20 (AMRESCO Inc.) to 1×10^6 particles/ml. The binary mixture was prepared by mixing 5- and 15-μm-diameter particles in a 1:1 ratio (volume/volume). Binary mixture of polystyrene particles was then introduced to the microchannel by using a syringe pump connected to the inlet plastic tube. The flow rate inside the microchannels was controlled by adjusting the setting of the pump.

In the experiment of tumor and blood cell separation, the channel was first filled with 1 × phosphate buffered saline (PBS). HeLa cells (human carcinoma cell line, average diameter around 13 μm) were grown to confluence in high-glucose Dulbecco's modified Eagle's medium (DMEM) supplemented with 10% fetal bovine serum (FBS) and 1% penicillin/streptomycin in a 5% CO_2, 37 °C incubator (Thermo Scientific). The cultured HeLa cells were stained with C3099 (0.5%, green) for about 1 h, followed by centrifuging at 1000 rpm for 3 min, and resuspending in 1 × PBS. The concentration of stained HeLa cells counted by a hemocytometer was

around 2×10^6 particles/ml. Human whole blood was drawn from healthy volunteers, and diluted 1:20 with $1 \times$ PBS to a cell concentration of 2.5×10^8 cells/ml. To model the low events of CTCs in blood, we spiked a small amount of fluorescently labeled HeLa cells into unstained $20 \times$ diluted blood to achieve a tumor-to-blood cell ratio of 8×10^{-7}. The prepared cell solution was introduced to the double spiral microchannel via the pump. The assembled device was mounted onto the stage of a Leica DMI 6000 microscope (Leica Microsystems). Optical and fluorescent microscope images were obtained by a CCD camera. The superimposed images were created automatically using Leica Application Suite (Leica Microsystems). The image analysis software Image-Pro Plus (Media Cybernetics) was used to measure the fluorescent intensity of captured images.

IV. RESULTS AND DISCUSSION

A. Numerical results

We begin with the CFD simulation of flow fields and particle motions in the 6-loop double spiral microchannel with one inlet and three outlets, as shown in Fig. 1. The three-dimensional computational domain was divided into more than 1×10^6 hexahedral meshes. The grid independency was tested by doubling the number of meshes and no discernible difference was found in simulation results using different meshes. We calculated the particle motions under various flow rates from 10 ml/h to 60 ml/h. Presence of the secondary Dean flow and their extent in the spiral microchannel were confirmed by numerical simulations. Fig. 2 shows the Dean flow within the S-shape junction at the flow rate of 10 ml/h and 60 ml/h, indicating a reversal in the direction of the Dean vortex for consecutive counterclockwise and clockwise spirals. At both flow rates, two counter-rotating Dean vortices form in the top and bottom halves of the channel. As expected, the magnitude of these Dean vortices proportionally increases with the flow rate, i.e., the channel Reynolds number.

Fig. 3 displays the trajectories of 5 μm diameter particles and 15 μm diameter particles under different flow rates ranging from 10 to 60 ml/h. As can be seen in Fig. 3, the large 15 μm particles are focused into a thin stream while the small 5 μm particles spread over a wide region of the cross-section. For 5 μm particles with $a/D_h < 0.07$, the Dean drag exceeds the inertial

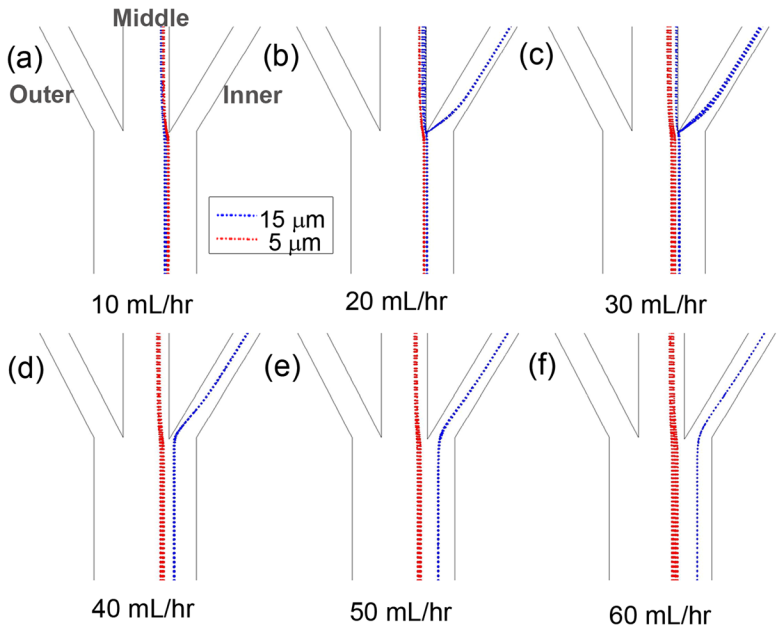

FIG. 3. Simulating prediction of trajectories of two types of particles near the inner/middle/outer outlet of the double spiral microchannel. (a) Flow rate 10 ml/h; (b) flow rate 20 ml/h; (c) flow rate 30 ml/h; (d) flow rate 40 ml/h; (e) flow rate 50 ml/h; (f) flow rate 60 ml/h. The red and blue dashed lines denote 5 μm particles and 15 μm particles, respectively.

lift regardless of the flow rates, resulting in the 5 μm particles getting entrained in the Dean vortices and a loss of particle focusing.[22,31] For 15 μm particles, the dominant inertial lift quickly aligns the particles to their equilibrium positions. We also note that the equilibrium positions of 15 μm particles shift closer to the inner channel wall with the increased flow rate and Re number. This phenomenon is manifested as the predominant inertial lift tends to push the particles towards the channel wall with the increasing Re.[26,32] These numerical results agree well with the experimental observations conducted in the same microchannel configuration and operating conditions (see Fig. 5 in Subsection IV B).

We also plot the global view of the trajectories of two types of particles along the double spiral channel at the flow rate of 60 ml/h in Fig. 4. This numerical predication suggests that for 15 μm particles, there exist three migration stages. When randomly distributed 15 μm particles enter the double spiral channel from the inlet, the dominant inertial lift rapidly aligns the particles to a thin stream, of which the equilibrium positions are toward to the inner channel wall (Stage I).[27] As particles flow close to the S-shape junction at the channel center, the enhanced Dean drag due to the increasing curvature radius and Dean number pushes the 15 μm particle-stream away from the channel wall (Stage II).[33] With particles flowing outward along the second spiral, the inertial lift becomes predominant again due to the gradually decreased Dean drag along the decreasing radius, leading to the final equilibrium positions of 15 μm particles near the inner channel wall (stage III). In comparison, 5 μm particles are prone to be influenced by the Dean drag, and thus, slowly equilibrate to their final positions toward the channel center after migrating a long distance.[22]

B. Separation of binary particle mixture

We first characterized the performance of the double spiral microfluidic cell sorter by separating the binary particle mixture. To visualize the trajectories of the particle movement, we used the mixture of green-stained 15 μm particles and red-stained 5 μm particles. The flow rate of the particle mixture that was 10, 20, 30, 40, 50, or 60 ml/h, was controlled by a syringe pump. The Reynolds number of 18, 35, 53, 71, 89, or 106, and the Dean number of 1.8, 3.6, 5.4, 7.2, 9.0, or 10.8 were derived from the above flow rate (Table I). Figs. 5(a)–5(f) show the superimposed fluorescent images of 5 μm (red line) and 15 μm (green line) particles at the S-shape junction at various flow rates. Fig. 5(g) plots the distribution and position of 15 μm (green) and 5 μm particle (red) at the center. The fluorescent green streaks in Fig. 5 reveal that the initially randomly dispersed 15 μm particles are concentrated to a narrow band of approximately 50 μm wide after particles traverse the first 6-loop spiral channel. Also, as the flow rate increases, the position of the streak moves closer to the midline of the channel. In comparison, the 5 μm particles cannot be ordered to a focused steam, thus, forming a broad fluorescent red

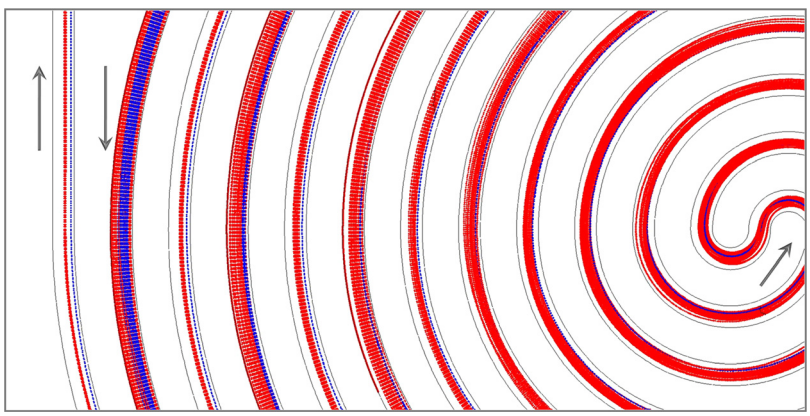

FIG. 4. Numerical prediction of the trajectories of 5 - and 15 -μm particles along the double spiral channel at the flow rate of 60 ml/h. The red and blue dashed lines denote 5 μm particles and 15 μm particles, respectively. The arrow represents the flow direction.

TABLE I. The statistical results of particle purity in the inner and the middle outlets of the double/single spiral microchannel for separating binary mixture of 5- and 15-μm particles.

			Double spiral		Single spiral	
Flow rate (ml/h)	Re number	Dean number	Inner outlet	Middle outlet	Inner outlets	Middle outlet
10	18	1.8	53.85 ± 4.63	55.43 ± 6.61	45.57 ± 4.51	55.46 ± 6.15
20	35	3.6	73.13 ± 1.66	81.46 ± 1.33	63.14 ± 2.93	75.59 ± 1.61
30	53	5.4	84.00 ± 2.95	85.74 ± 0.52	72.50 ± 1.34	79.39 ± 1.13
40	71	7.2	95.14 ± 2.70	97.34 ± 2.07	88.80 ± 2.67	86.82 ± 3.54
50	89	9.0	98.72 ± 0.87	97.95 ± 1.55	90.68 ± 1.67	88.71 ± 2.36
60	106	10.8	98.04 ± 0.71	97.28 ± 1.19	89.80 ± 2.37	89.81 ± 2.58

streak wider than 150 μm at the center junction. After particles pass the S-shape junction, they continue to migrate along the clockwise direction to the trifurcated outlet. At a low flow rate of 10 ml/h, most 5 - and 15 -μm particles flow out from the middle outlet (Figs. 5(a′)–5(f′)). As the flow rate increases, the stream of 15 μm particles is deflected toward the inner outlet, while

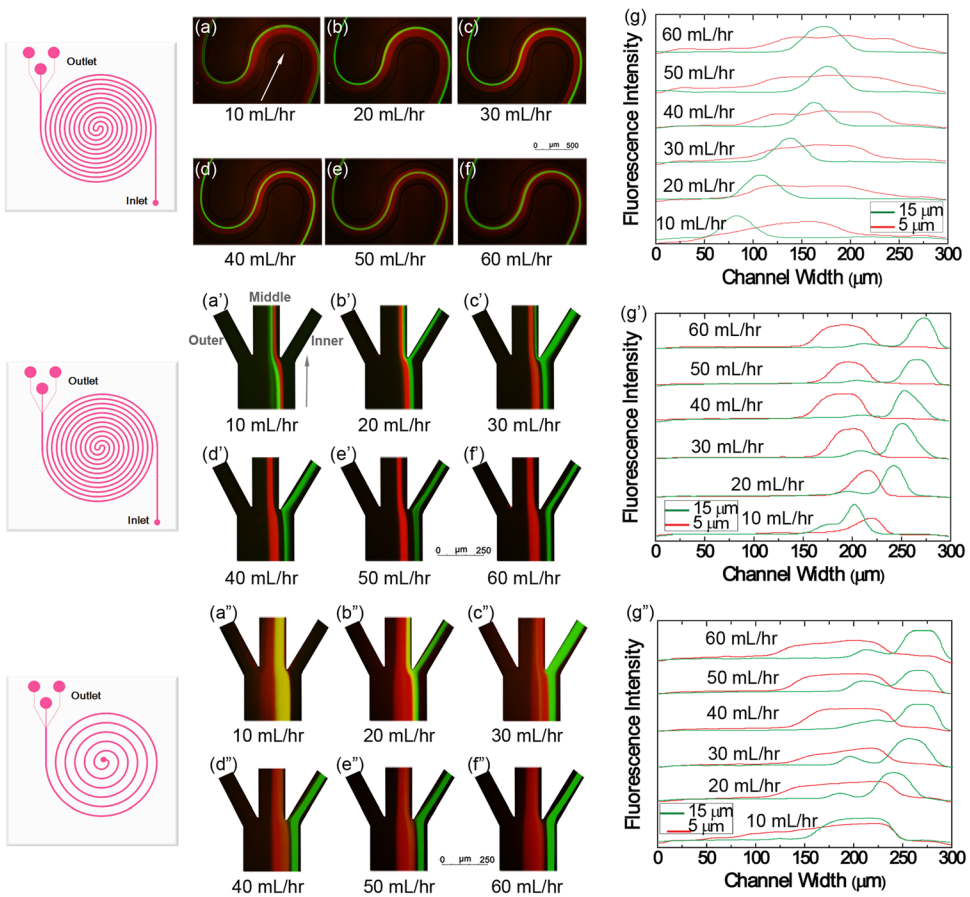

FIG. 5. (a)–(f) Superimposed fluorescent images at the center of the double spiral channel for 5 μm (red line) and 15 μm (green line) particles at six different flow rates ranging from 10 to 60 ml/h. The arrow indicates the flow direction. (g) Line scans across the 300 μm wide channel of each composite image taken at the center to illustrate the distribution and position of 5 μm and 15 μm particles. (a′)–(f′) Superimposed fluorescent images at the outlet of the double spiral channel for 5 μm (red line) and 15 μm (green line) particles at the same flow rates. (g′) Line scans across the 300 μm wide channel of each composite image taken at the outlet. (a″)–(f″) Superimposed fluorescent images at the outlet of the single spiral channel. (g″) Line scans across the outlet of the single spiral channel.

most 5 μm particles still migrate out through the middle outlet with steam width around 75 μm. We also observe that the steam of 15 μm particle (green) moves closer to the inner channel wall with the increased flow rate at the outlet. In this way, an effective separation of the binary mixture is achieved at the flow rates of 40 ml/h and above. These experimental observations are consistent with the numerical prediction in Sec. IV A. To demonstrate the comparison between the double spiral and single spiral designs, we performed the particle separation experiments using the single spiral channel at the same flow rate ranging from 10 to 60 ml/h (Figs. 5(a″)–5(g″)). As expected, the distribution and the position of 15 μm particles are similar to that in the double spiral, as the dominant lift force will order the 15 μm particles to their equilibrium positions toward the inner channel wall in a short time (Figs. 5(a″)–5(g″)). However, the 5 μm particles cannot be concentrated to a narrow band due to the weak inertial lift and the short migration length (Figs. 5(a″)–5(g″)).

We note that in the S-shape center junction of the double spiral channel, Dean vortices are enhanced due to the small radius, which might disturb the ordered distribution of particles. However, such negative effect can be neglected as particles rapidly traverse the S-shape junction. Moreover, the second spiral provides an extra channel length of 167 mm for particle migration in the limited chip space. When ordering 5 μm particles subjected to the weak inertial lift, the sufficient migration length with the decreased Dean drag assists in the focusing and separation performance of small particles. We also observe that the channel height has a dramatic influence on equilibrium positions and focusing performance of particles inside the double spiral channel. For example, at the Reynolds number of around 50 and channel height of 50 μm, the small particles (5 -μm in diameter) converge to a well-focused stream with equilibrium positions close to the inner channel wall.[24] If the channel height increases to 85 μm with other parameters unchanged, small particles equilibrate around the channel center and concentrate to a broad stream. In comparison, the large particles (15 -μm in diameter) alter their equilibrium positions from channel midline toward the inner channel wall with the increased channel height from 50 μm to 85 μm. In addition, the 85 μm high channel can sustain a high flow rate up to 60 ml/h, while the 50 μm high channel is prone to leakage if the flow rate is higher than 30 ml/h. The dynamic mechanism of the particle motion in the curved microchannel is very complex and not conclusive yet. We will conduct more systematic investigation in the future study.

To quantitatively assess the separation performance of the single and the double spiral channel, we captured the microscopic images of fluorescent particles and counted more than 500 particles at the inner and middle outlets for each flow rate ranging from 10 to 60 ml/h. If we define a complete separation as all 15 μm particles migrate to the inner outlet and 5 μm particles move to the middle outlet, the separation purity is given by the ratio of the number of one type of particles collected at the desired outlet (the inner outlet for 15 μm particles or the middle outlet for 5 μm particles) to the total number of particles in that outlet. The calculated purity at the inner and the middle outlets versus the flow rate is shown in Table. I. The percentage of 15 μm particles in the inner outlet of the double spiral channel increases from 53.85% to 98.72%, and the percentage of 5 μm particles in the middle outlet of the double spiral channel also increases from 55.43% to 97.95% with the enhanced flow rate from 10 to 60 ml/h. Based on the characterization results, a complete particle separation is accomplished at the flow rate above 30 ml/h for double spiral channel. In comparison, the purity at the outlets of the single spiral channel is approximately 10% lower than that from the double spiral at the flow rate above 30 ml/h (Table I).

C. Separation of HeLa cells from human blood cells

The 6-loop double spiral microchannel was also applied to separate HeLa cells from 20 × diluted human blood cells. The blood samples from volunteers mainly contain erythrocytes that are 8 μm biconcave disks and peripheral blood lymphocytes that are 7–10 μm in diameter. The cultured HeLa cells have an average diameter around 13 μm. The size difference between tumor and blood cells is the key factor for hydrodynamic cell separation. To visualize the

trajectories of cells, we captured and superimposed the fluorescent microscope images of HeLa cells (green stream) and the optical microscope images of blood cells (dark stream) at the trifurcated outlet (Fig. 6). At the flow rate of 40 ml/h, a small fraction of blood cells is deflected to the inner outlet (Fig. 6(a)), while some HeLa cells traverse to the middle outlet of the double spiral channel (Fig. 6(b)), revealing an uncompleted separation (Fig. 6(c)). Most peripheral lymphocytes of diameter ranging from 7 to10 μm have the similar equilibrium positions of the red blood cells, thus, migrating out from the middle outlet. However, a few white blood cells with comparable sizes to tumor cells can be isolated from the red blood cells, and traverse toward the inner outlet with the spiked HeLa cells. This separation result is worse than that of the binary particle at the same flow rate because: (1) the size difference between HeLa and blood cells is smaller than that between 15- and 5-μm particles; (2) both types of cells have large variations in cell sizes; (3) the increased blood concentration results in the enhanced cell-cell interaction and the consequent focusing dispersion. As the flow rate increases to 60 ml/h (Figs. 6(a′)–6(c′)), the focused blood stream flows out from the middle outlet, and almost the entire stream of HeLa cells is reflected to the inner outlet. We suggest that the increased flow rate and Reynolds number results in the increased dominance of the lift force to compete with the Dean drag acting on cells, thus, separating the HeLa cells from blood samples based on their size-dependent equilibrium positions. Also, the gradually decreased Dean drag force inside

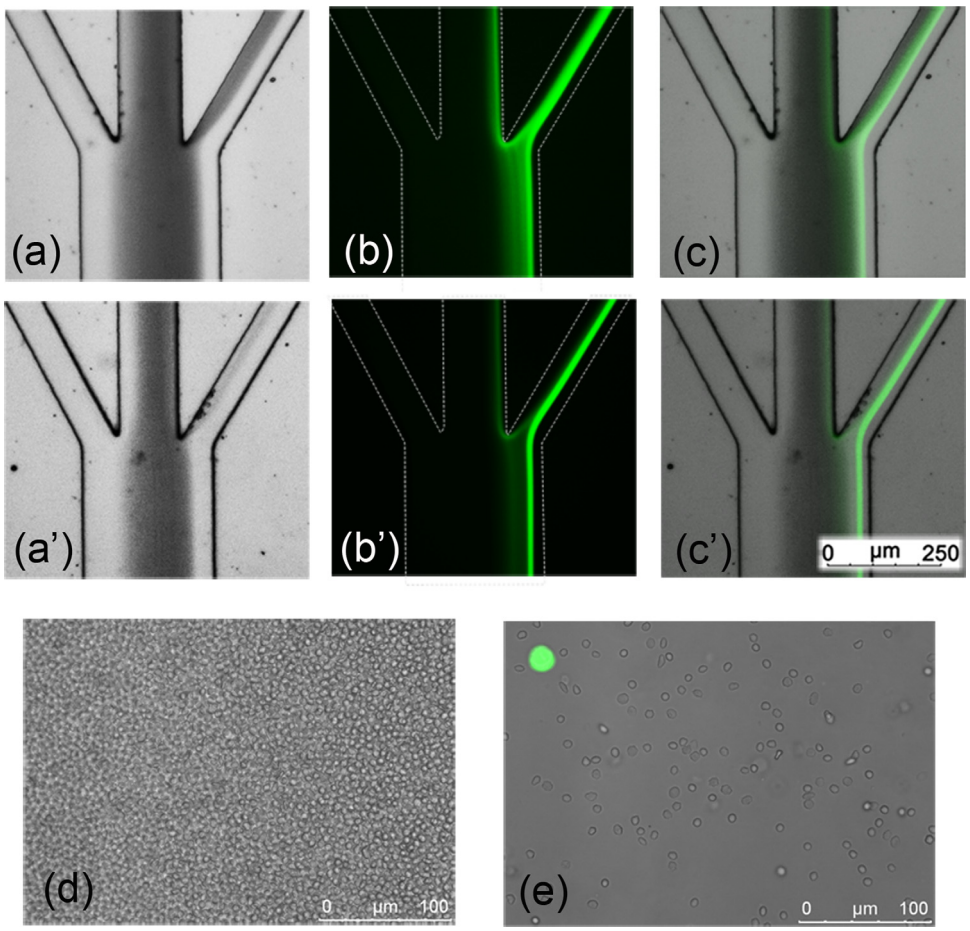

FIG. 6. (a) The optical microscope image indicating the trajectories of blood cells, (b) the fluorescent microscope image of HeLa cells, and (c) the superimposed image at the outlet of the double spiral channel at 40 ml/h. HeLa cells are stained with green and 20 × diluted blood cells are unstained. (a′)–(c′) The optical, fluorescent and superimposed microscope images taken at the outlet of the double spiral channel at 60 ml/h. (d) The composite image of cells collected at the middle outlet of the double spiral at 60 ml/h. (e) The composite image of cells collected at the inner outlet at 60 ml/h.

the second spiral of the double spiral geometry plays a key role in ordering the HeLa and blood cells to two focused streams at the outlet.

To mimic the CTC separation from blood cells, we prepared the blood samples with spiked HeLa cells. The initial tumor-to-blood cell ratio was 8×10^{-7}, and the cell concentration of the blood sample was around 2.5×10^{8} cells/ml. The blood sample was introduced to the double spiral channel using a syringe pump at 60 ml/h. The superimposed microscope images of cells collected at the middle outlet and the inner outlet are shown in Figs. 6(d) and 6(e), respectively, in which HeLa cells are stained with green and 20 × diluted blood cells are unstained. By analyzing 1 ml collected sample after separation using the double spiral channel, we estimate that the separation efficiency is $91.32 \pm 2.09\%$ for blood cells, and $90.54 \pm 3.41\%$ for HeLa cells at 60 ml/h with the throughput of 2.5×10^{8} cells/min. The separation efficiency is defined as the ratio of the number of one type of cells collected at the desired outlet (the inner outlet for HeLa cells or the middle outlet for blood cells) to the total number of this kind of cells at all outlets. By counting the numbers of green-stained HeLa cells before and after separation, we obtain a tumor recovery rate of around 80%. We also note that the green-stained HeLa cells at the inner outlet keep their intact spherical shape without noticeable cell damage, indicating a possibility for further cell culture and analysis.[34]

Although the cell separation efficiency in the current double spiral channel is slightly lower compared to immuno-binding methods or microfluidic filtration, the hydrodynamic microfluidic technique provides a new way for label-free and size-based tumor cell separation with a high throughput.[35] The passive cell separation technique also allows easy retrieval of target cells that remain viable and intact, which could be used for further cell culture and gene analysis. Compared to other hydrodynamic sorting devices using the curved serpentine and the side branch channels, our double spiral design has an excellent separation efficiency of more than 90% and a high cell throughput of 1.5×10^{10} cells/h (corresponding to 3 ml whole blood per hour).[13,21] In order to enhance the separation efficiency, designing of multiplex cascading of separation circuits or integration of a chip-based detection downstream to refine the collected cells should be attempted in future study.

V. CONCLUSIONS

In this work, we presented a double spiral microfluidic device that rapidly separates particles or cells in a label-free manner by using the hydrodynamic forces inside the curved geometry. A numerical simulation has been performed to predict the particle movement inside the double spiral microchannel. Substantial investigations of hydrodynamic particle separation indicated a separation purity of 98%. Separation of HeLa and 20 × diluted blood samples at the initial tumor-to-blood cell ratio of 8×10^{-7} was achieved by using the double spiral design. We expect this microfluidic platform driven by purely hydrodynamic forces would have an impact on detection and fundamental studies of circulating tumor cells in future.

ACKNOWLEDGMENTS

J.S. and X.J. acknowledge financial support from MOST (2011CB933201, 2009CB930001), NSFC (51105086, 21025520, and 90813032), and CAS (KJCX2-YW-M15). G.H. acknowledges financial support from MOST (2011CB707604), NSFC (50890182), and CAS (KJCX2-YW-H18).

[1]R. T. Krivacic, A. Ladanyi, D. N. Curry, H. B. Hsieh, P. Kuhn, D. E. Bergsrud, J. F. Kepros, T. Barbera, M. Y. Ho, L. B. Chen, R. A. Lerner, and R. H. Bruce, Proc. Natl. Acad. Sci. U.S.A. **101**, 10501 (2004).
[2]M. E. Vincent, W. S. Liu, E. B. Haney, and R. F. Ismagilov, Chem. Soc. Rev. **39**, 974 (2010).
[3]D. F. Hayes, M. C. Miller, M. Cristofanilli, M. J. Ellis, A. Stopek, W. J. Allard, J. Matera, G. V. Doyle, L. W. W. M. Terstappen, and G. T. Budd, Breast Cancer Res. Treat. **88**, S225 (2004).
[4]D. W. Bell and D. A. Haber, Clin. Cancer Res. **12**, 3875 (2006).
[5]B. Mostert, S. Sleijfer, J. A. Foekens, and J. W. Gratama, Cancer Treat. Rev. **35**, 463 (2009).
[6]J. Sun, Y. Gao, R. J. Isaacs, K. C. Boelte, C. P. Lin, E. M. Boczko, and D. Li, Anal. Chem. **84**, 2017 (2012).
[7]L. Wang, Z. L. Zhang, J. Wdzieczak-Bakala, D. W. Pang, J. M. Liu, and Y. Chen, Lab Chip **11**, 4235 (2011).
[8]Y. Ai, S. W. Joo, Y. T. Jiang, X. C. Xuan, and S. Z. Qian, Biomicrofluidics **3**, 022404 (2009).
[9]H. Tsutsui and C. M. Ho, Mech. Res. Commun. **36**, 92 (2009).

[10]N. Pamme, Lab Chip **7**, 1644 (2007).
[11]J. J. Zhu and X. C. Xuan, Biomicrofluidics **5**, 024111 (2011).
[12]G. D. Chen, F. Fachin, M. Fernandez-Suarez, B. L. Wardle, and M. Toner, Small **7**, 1061 (2011).
[13]A. A. S. Bhagat, H. W. Hou, L. D. Li, J. Y. Han, and C. T. Lim, Lab Chip **11**, 1870 (2011).
[14]S. Zheng, H. Lin, J. Q. Liu, M. Balic, R. Datar, R. J. Cote, and Y. C. Tai, J. Chromatogr. A **1162**, 154 (2007).
[15]S. Y. Zheng, H. K. Lin, B. Lu, A. Williams, R. Datar, R. J. Cote, and Y. C. Tai, Biomed. Microdevices **13**, 203 (2011).
[16]S. J. Tan, L. Yobas, G. Y. H. Lee, C. N. Ong, and C. T. Lim, Biomed. Microdevices **11**, 883 (2009).
[17]D. Wlodkowic and J. M. Cooper, Curr. Opin. Chem. Biol. **14**, 556 (2010).
[18]B. D. Plouffe, L. H. Lewis, and S. K. Murthy, Biomicrofluidics **5**, 013413 (2011).
[19]Y. Liu, D. Hartono, and K. M. Lim, Biomicrofluidics **6**, 012802 (2012).
[20]Y. Kang, D. Li, S. A. Kalams, and J. E. Eid, Biomed. Microdevices **10**, 243 (2008).
[21]S. C. Hur, A. J. Mach, and D. Di Carlo, Biomicrofluidics **5**, 022206 (2011).
[22]D. Di Carlo, D. Irimia, R. G. Tompkins, and M. Toner, Proc. Natl. Acad. Sci. U.S.A. **104**, 18892 (2007).
[23]S. S. Kuntaegowdanahalli, A. A. S. Bhagat, G. Kumar, and I. Papautsky, Lab Chip **9**, 2973 (2009).
[24]J. Sun, M. Li, C. Liu, Y. Zhang, D. Liu, W. Liu, G. Hu, and X. Jiang, Lab Chip **12**, 3952 (2012).
[25]J. A. Schonberg and E. J. Hinch, J. Fluid Mech. **203**, 517 (1989).
[26]E. S. Asmolov, J. Fluid Mech. **381**, 63 (1999).
[27]D. Di Carlo, J. F. Edd, K. J. Humphry, H. A. Stone, and M. Toner, Phys. Rev. Lett. **102**, 094503 (2009).
[28]B. Yuan, Y. Jin, Y. Sun, D. Wang, J. S. Sun, Z. Wang, W. Zhang, and X. Y. Jiang, Adv. Mater. **24**, 890 (2012).
[29]J. Sun, C. C. Stowers, E. M. Boczko, and D. Li, Lab Chip **10**, 2986 (2010).
[30]J. S. Sun, S. K. Vajandar, D. Y. Xu, Y. J. Kang, G. Q. Hu, D. Q. Li, and D. Y. Li, Microfluid. Nanofluid. **6**, 589 (2009).
[31]A. A. S. Bhagat, S. S. Kuntaegowdanahalli, and I. Papautsky, Lab Chip **8**, 1906 (2008).
[32]J. P. Matas, J. F. Morris, and E. Guazzelli, J. Fluid Mech. **515**, 171 (2004).
[33]D. R. Gossett and D. Di Carlo, Anal. Chem. **81**, 8459 (2009).
[34]S. C. Hur, N. K. Henderson-MacLennan, E. R. B. McCabe, and D. Di Carlo, Lab Chip **11**, 912 (2011).
[35]J. P. Gleghorn, E. D. Pratt, D. Denning, H. Liu, N. H. Bander, S. T. Tagawa, D. M. Nanus, P. A. Giannakakou, and B. J. Kirby, Lab Chip **10**, 27 (2010).